

# Electrochemistry of Selenium with Sodium and Lithium: Kinetics and Reaction Mechanism

Qianqian Li,<sup>†,‡</sup> Huguang Liu,<sup>†,‡,⊥</sup> Zhenpeng Yao,<sup>†</sup> Jipeng Cheng,<sup>†,‡,§</sup> Tiehu Li,<sup>⊥</sup> Yuan Li,<sup>†,‡</sup> Chris Wolverton,<sup>†</sup> Jinsong Wu,<sup>\*,†,‡</sup> and Vinayak P. Dravid<sup>\*,†,‡</sup>

<sup>†</sup>Department of Materials Science and Engineering and <sup>‡</sup>The NUANCE Center, Northwestern University, Evanston, Illinois 60208, United States

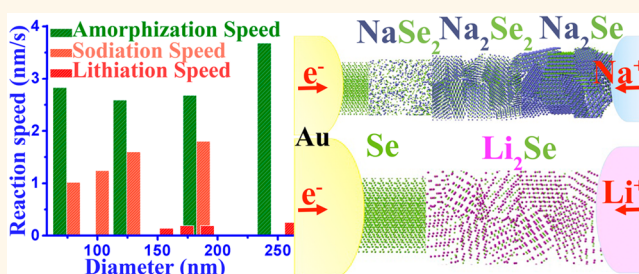
<sup>§</sup>School of Materials Science & Engineering, Zhejiang University, Hangzhou 310027, People's Republic of China

<sup>⊥</sup>Department of Materials Science and Engineering, Northwestern Polytechnical University, Xi'an 710072, People's Republic of China

## Supporting Information

**ABSTRACT:** There are economic and environmental advantages by replacing Li with Na in energy storage. However, sluggishness in the charge/discharge reaction and low capacity are among the major obstacles to development of high-power sodium-ion batteries. Among the electrode materials recently developed for sodium-ion batteries, selenium shows considerable promise because of its high capacity and good cycling ability. Herein, we have investigated the mechanism and kinetics of both sodiation and lithiation reactions with selenium nanotubes, using *in situ* transmission electron microscopy. Sodiation of a selenium nanotube exhibits a three-step reaction mechanism: (1) the selenium single crystal transforms into an amorphous phase Na<sub>0.5</sub>Se; (2) the Na<sub>0.5</sub>Se amorphous phase crystallizes to form a polycrystalline Na<sub>2</sub>Se<sub>2</sub> phase; and (3) Na<sub>2</sub>Se<sub>2</sub> transforms into the Na<sub>2</sub>Se phase. Under similar conditions, the lithiation of Se exhibits a one-step reaction mechanism, with phase transformation from single-crystalline Se to a Li<sub>2</sub>Se. Intriguingly, sodiation kinetics is generally about 4–5 times faster than that of lithiation, and the kinetics during the different stages of sodiation is different. Na-based intermediate phases are found to have improved electronic and ionic conductivity compared to those of Li compounds by first-principles density functional theory calculations.

**KEYWORDS:** *in situ* transmission electron microscopy, sodium-ion battery, selenium cathodes, lithium-ion battery, alloying reaction, *in situ* electron diffraction, DFT calculation



Sodium-ion batteries have recently attracted worldwide attention for renewable energy grid storage and electric vehicles due to the intrinsic advantages of sodium: it is environmentally benign, has lower cost, and has relative abundance.<sup>1,2</sup> If sodium-ion batteries can be a commercial substitute for lithium-ion batteries in daily life, cost could be reduced by nearly 30%, while ensuring greater sustainability.<sup>3</sup> Historically, high-temperature Na–S batteries have been developed as one of several promising technologies for large-scale renewable energy storage because of its high theoretical specific energy, high-energy efficiency, and good cycle life.<sup>4–6</sup> Although the technology has already been produced commercially and tested for grid storage, its high operation temperature (*e.g.*, 300–350 °C)<sup>7</sup> is the major disadvantage. It significantly increases the cost of battery manufacturing and maintenance and causes safety concerns. Indeed, sodium-ion batteries operated at room temperature would be promising if appropriate electrode materials can be discovered.

Work to develop useful electrodes for sodium-ion batteries can be traced back to the first discovery of lithium-ion

batteries.<sup>8,9</sup> This research was quickly dropped due to the sluggish reaction with Na and the low capacity of most intercalated electrode materials that worked efficiently with lithium-ion electrochemistry. The diameter of a sodium ion (0.95 Å) is much larger than that of lithium ion (0.68 Å), which prevents Na ions from intercalating into most intercalating electrodes. Recently, several types of high-capacity anode materials with either conversion or alloy reaction with Na have been discovered, such as black phosphorus,<sup>10</sup> SnP<sub>3</sub>.<sup>11</sup>

Based on alloying reactions, selenium shows promising electrochemical performance as a cathode with both Li and Na, capable of room temperature cycling (up to 4.6 V) without failure.<sup>12</sup> Selenium has an electrical conductivity ( $1 \times 10^{-3} \text{ S m}^{-1}$ ) much higher than that of sulfur ( $5 \times 10^{-28} \text{ S m}^{-1}$ ), and its volumetric capacity is as high as that of sulfur cathode material.<sup>12,13</sup> Combining Se with carbon, in particular, may

Received: July 7, 2016

Accepted: August 26, 2016

Published: August 26, 2016

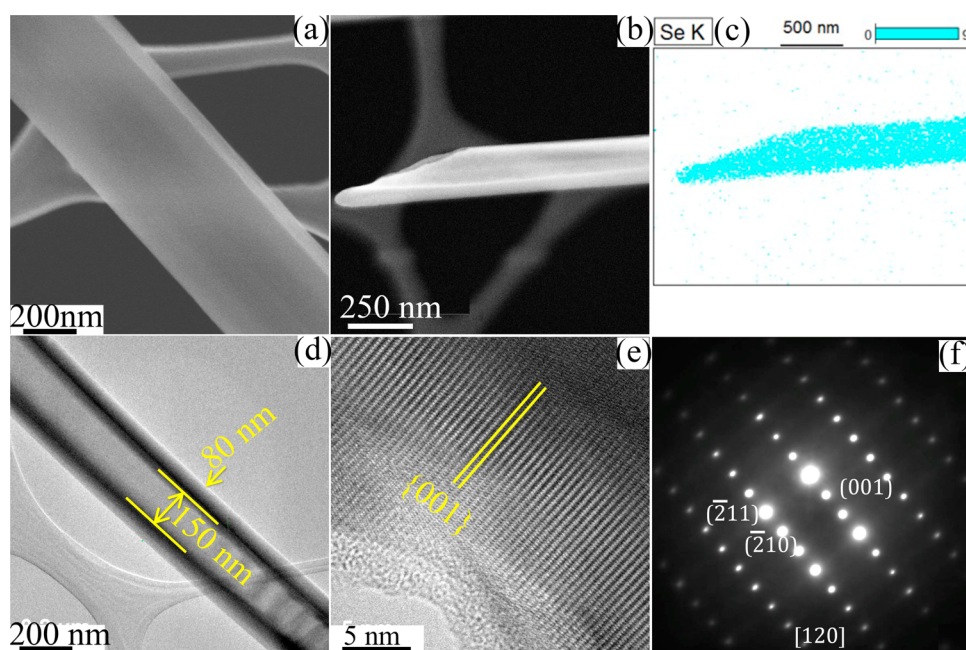


**Figure 1.** Basic microstructure characterization of the selenium nanotube by SEM, STEM, and TEM. (a) Typical SEM image shows the trigonal structure, and the inset image is the schematic image of the selenium nanotube. (b) STEM image of one single selenium nanotube. (c) EDS map was taken from the region of (b). (d) TEM image shows the tube microstructure with a wall thickness of  $\sim 80$  nm and the diameter of tube part of  $\sim 150$  nm. (e) High-resolution TEM image shows that the growth direction of this nanotube is along the  $[001]$ . (f) Electron diffraction pattern indicates one single selenium has an excellent single-crystalline microstructure.

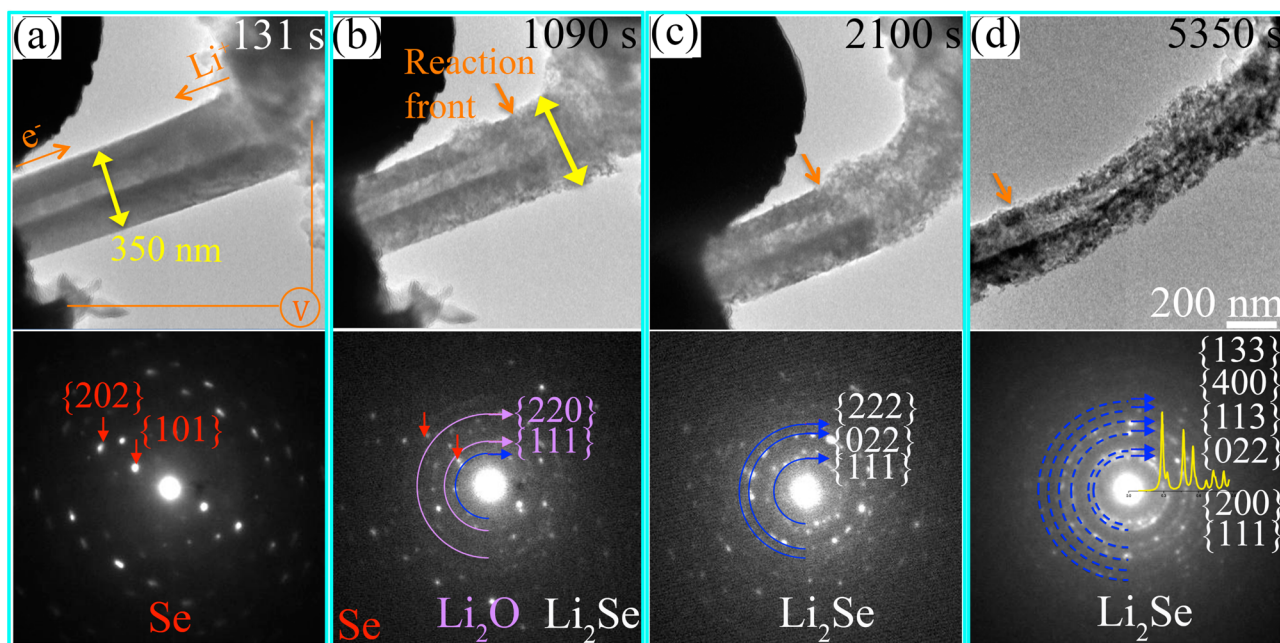


**Figure 2.** Evolution of morphology and microstructure of a selenium nanotube in the lithiation process. A nanobattery was built inside the TEM with selenium as the cathode, lithium metal as the anode, and  $\text{Li}_2\text{O}$  grown on the surface of lithium metal as the solid electrolyte. When a bias of  $-3$  V is applied, a lithiation process is triggered. (a–d) Top row shows the morphological evolution of the Se nanotube in the lithiation. Bottom row shows the dynamic electron diffraction patterns. The diffraction rings of  $\text{Li}_2\text{O}$  in (b) may due to fast surface diffusion of  $\text{Li}_2\text{O}$ . The diffraction rings of the  $\text{Li}_2\text{Se}$  phase are labeled by blue half circles. The simulated powder diffraction pattern shown in the line profile is inset in (d).

significantly improve the cycle performance and Coulombic efficiency of the selenium cathode due to the increasing electronic and ionic conductivities.<sup>14–16</sup>

However, different reaction pathways have been observed when the cells are run with different electrolytes.<sup>13,15,17</sup> A

detailed mechanism of the alloying reactions with selenium during cycling remains unclear. It is especially unclear why the electrochemical properties of Se in sodium-ion batteries are as good as those in lithium-ion batteries. Here, we report real-time observations of the alloying reactions of selenium with sodium

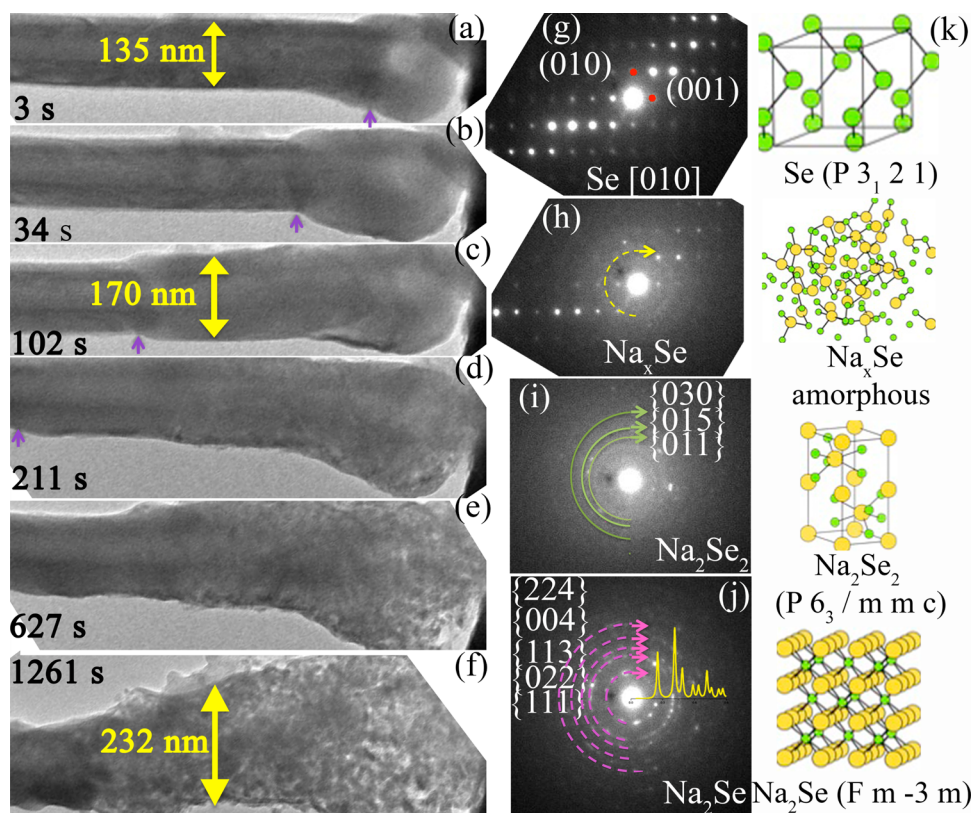


**Figure 3.** Reaction mechanism and phase transformation of the Se nanotube during the sodiation process. (a–f) Morphological evolution of the individual selenium nanotube in the sodiation process. The diameter of this nanotube expands from 135 to 170 nm with volume expansion of 58% in the first step and further expands to 232 nm with overall volume expansion of 336%. (g–j) Evolution of electron diffraction patterns in the sodiation process. The phase transformations from Se single crystal to amorphous  $\text{Na}_x\text{Se}$  to polycrystalline  $\text{Na}_2\text{Se}_2$  and  $\text{Na}_2\text{Se}$  are identified. The green half circles show the simulated rings of the  $\text{Na}_2\text{Se}_2$  phase. The pink and dashed circles are the simulation electron diffraction rings of the  $\text{Na}_2\text{Se}$  phase, and the yellow curve exhibits their intensities. (k) Illustration of the atomic structures of Se, amorphous  $\text{Na}_x\text{Se}$ , crystalline  $\text{Na}_2\text{Se}_2$ , and  $\text{Na}_2\text{Se}$  phases appearing in the sodiation process.

and lithium in similar experimental settings using *in situ* transmission electron microscopy (TEM). The reactions of Se with Na and Li are mutually compared at high spatial resolution during the dynamical sodiation and lithiation processes. In addition to the reaction mechanism of selenium in sodium- and lithium-ion batteries, the reaction kinetics is also investigated by directly measuring the reaction speed at the nanoscale. The underlying mechanisms are then further explored by density functional theory (DFT) calculations with consideration of the crystalline structure, reaction thermodynamic energies, band gaps, and ion diffusivities.

## RESULTS AND DISCUSSION

Selenium nanotubes have been successfully synthesized by a simple hydrothermal method. The crystallographic structure and phase purity of the as-prepared selenium nanotubes were analyzed by X-ray diffraction (XRD). As shown in Figure S1, all characteristic diffraction peaks in the XRD pattern can be indexed as a single selenium phase (JCPDS 06-0362), with trigonal lattice  $a = 4.366 \text{ \AA}$ ,  $b = 4.366 \text{ \AA}$ ,  $c = 4.956 \text{ \AA}$ ,  $\alpha = 90^\circ$ ,  $\beta = 90^\circ$ ,  $\gamma = 120^\circ$ , and a space group of  $P3_121$  with spiral chain structure. The typical morphology of a selenium nanotube with clear facets is revealed by the scanning electron microscope (SEM) image in Figure 1a. Figure 1b is a scanning transmission electron microscopy (STEM) image with Z-contrast of a selenium nanotube. A Se map collected by energy-dispersive X-ray spectroscopy (EDS) verifies the chemical composition of

the nanotube, as shown in Figure 1c. A typical TEM image in Figure 1d shows clearly the hollow structure of the nanotube with brighter contrast in the middle. The diameter of the nanotube region is about 310 nm, and the wall of the nanotube is about 80 nm thick. The tube axis is along the [001] direction, as shown in Figure 1e, which is the high-resolution TEM image of the selenium tube. The selected area electron diffraction (SAED) pattern of the selenium nanotube along the [120] zone axis in Figure 1f reveals that an individual selenium nanotube has desirable single-crystalline structure.

The electrochemical reaction of Se and Li under bias was investigated by *in situ* TEM, and a single-step lithiation,  $\text{Se} + 2\text{Li} = \text{Li}_2\text{Se}$ , was observed. Figure 2a–d shows morphological evolutions of the Se nanotube during the lithiation process (Movie S1). The original 350 nm diameter of the nanotube is gradually expanded to 480 nm with a volume expansion of  $\sim 88\%$ . Meanwhile, the reaction front interface moves 1300 nm forward in 5350 s, corresponding to a reaction speed of  $\sim 0.25 \text{ nm s}^{-1}$  (volume speed of  $3 \times 10^4 \text{ nm}^3 \text{ s}^{-1}$ ). The contrast changes in the unreacted Se area shown in Movie S1 may be caused by stress/strain due to surface reaction, volume expansion from the reacted area, and the electron beam illumination. The crystalline phase transformation during lithiation is also monitored by electron diffraction (Movie S2). It is found that the single-crystal selenium (Figure 2a) gradually transforms into polycrystalline  $\text{Li}_2\text{Se}$  phase (Figure 2b–d), marked by the blue half circles (Figure 2c). The

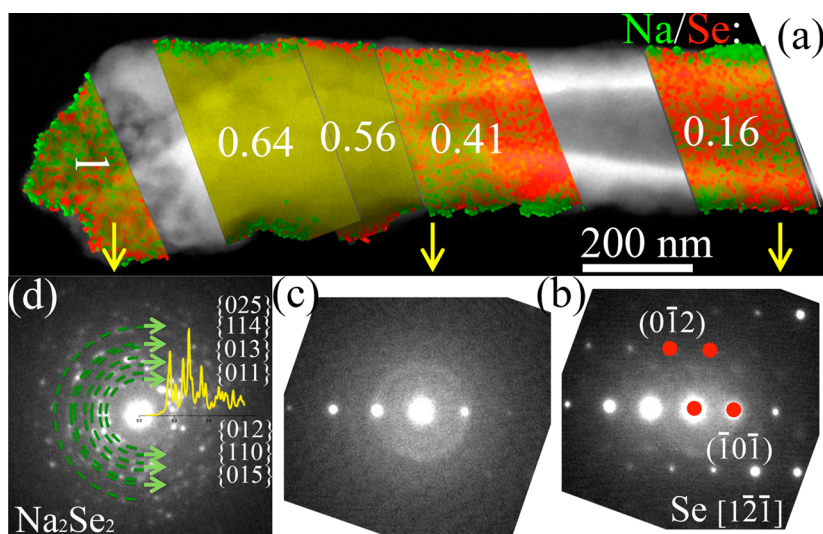


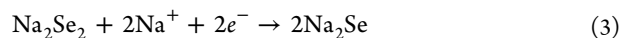
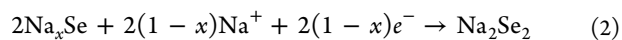
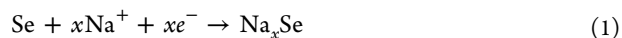
**Figure 4.** Identification of chemical composition of the amorphous phase. (a) STEM image of the partially sodiated selenium nanotube overlaid with the EDS map, where Na is represented as green and Se as red. (b–d) Electron diffraction patterns collected from different phase regions, confirming that they are single-crystalline Se, amorphous  $\text{Na}_x\text{Se}$ , and polycrystalline  $\text{Na}_2\text{Se}_2$ . In (d), the green dashed circles are the simulated rings of the  $\text{Na}_2\text{Se}_2$  phase, and the intensity of the rings is shown by the yellow curve.

electron diffraction pattern (EDP) simulation results of the  $\text{Li}_2\text{Se}$  phase (blue dashed half circles) match very well with our experimental data shown in Figure 2d. The intensity of the corresponding crystal plane is shown by the yellow curve in Figure 2d and Figure S5. In our experiments, we did not observe another intermediate phase in the lithiation process. The  $\text{Li}_2\text{O}$  phase identified from the electron diffraction pattern in Figure 2b likely originates from surface diffusion of  $\text{Li}_2\text{O}$  used as a solid electrolyte.

In contrast to a single-step reaction between Se and Li, a three-step reaction mechanism appears to prevail in the electrochemical reaction between Se and Na, as observed by *in situ* TEM. Figure 3a–f shows the evolution of an individual selenium nanotube’s morphology and microstructure during the first sodiation process (also in Movie S3). The selenium nanotube with an initial diameter of  $\sim 135$  nm expands to  $\sim 170$  nm, with corresponding volume expansion by  $\sim 58\%$ . The reaction front moves forward at an average speed of  $\sim 4.3$  nm  $\text{s}^{-1}$  (volumetric speed of  $8 \times 10^4$  nm $^3$   $\text{s}^{-1}$ ) in this stage (as marked by purple arrows in Figure 3a–d). It moves much quicker than that in the lithiation process. In the following sodiation process, many grain boundaries appear, indicating the formation of small crystalline nanoparticles. Meanwhile, the diameter of the nanotube expands to  $\sim 282$  nm, corresponding to a volume expansion of  $\sim 336\%$  (Figure 3d–f). While there is a large radial expansion, the length of the selenium nanotube remains almost unchanged.

Phase transformations in the sodiation process have been studied by analyzing the dynamic SAED patterns (Movie S4). A pristine Se nanotube is identified to be oriented close to the [010] zone axis, as shown in Figure 3g, where the spots of (001) and (010) are labeled. Upon sodiation, the diffraction spots of selenium slowly disappeared (Figure 3h), while a blurry diffraction halo starts to appear (Figure 3h), indicating that pristine Se gradually transforms into an amorphous phase, termed  $\text{Na}_x\text{Se}$ . With further sodiation and increase of sodium content in the amorphous  $\text{Na}_x\text{Se}$ , a recrystallization process is observed in the second stage of sodiation. As shown in Figure 3i, diffraction spots and rings appear, and they can be indexed

as the {011}, {015}, and {030} reflections of  $\text{Na}_2\text{Se}_2$ , a phase with a 1:1 Se to Na ratio. In the third stage, a phase transformation from  $\text{Na}_2\text{Se}_2$  to  $\text{Na}_2\text{Se}$  has been identified. After full sodiation, all of the Na-based intermediate phases completely transit to the  $\text{Na}_2\text{Se}$  phase, indicated by the EDP simulation results marked by the pink dashed half circles in the last diffraction pattern in Figure 3j. Here, one Se can host 2 Na atoms in the structure, and the theoretical capacity of the  $\text{Na}_2\text{Se}$  phase is 679 mAh/g. As revealed by electron diffraction, a three-step process consisting of amorphization, recrystallization, and solid-state phase transformation were observed in the Se sodiation. The recrystallization is accompanied by collapse of the Se nanotube with formation of nanocrystals of the Na–Se compounds. The following summarizes the three-step reaction:



We then applied EDS in STEM to determine the composition of the amorphous  $\text{Na}_x\text{Se}$  phase. In a partially sodiated selenium nanotube, as shown Figure 4a, three kinds of phases, including single-crystalline Se, amorphous  $\text{Na}_x\text{Se}$ , and polycrystalline  $\text{Na}_2\text{Se}_2$  phase, can be identified by their corresponding SAED patterns. The interfaces between different phases are clear due to their different diffraction contrasts. A straight nanotube is also bent, due to sodium insertion, and the expansions in their diameters are different at different regions, as shown in Figure 4a. The electron diffraction pattern in the single-crystalline Se region can be indexed along the [1–2–1] zone axis (Figure 4b). The surface of the amorphous  $\text{Na}_x\text{Se}$  phase, indicated by the corresponding SAED pattern (Figure 4c), becomes smooth, although it maintains a tubular morphology. Meanwhile, the  $\text{Na}_2\text{Se}_2$  phase can be identified by the diffraction ring patterns shown in the corresponding SAED pattern of Figure 4d, in which the {011}, {012}, {013}, and {110} rings are labeled by the green dashed half circles and arrows, which are the simulation of EDP of the  $\text{Na}_2\text{Se}_2$  phase,

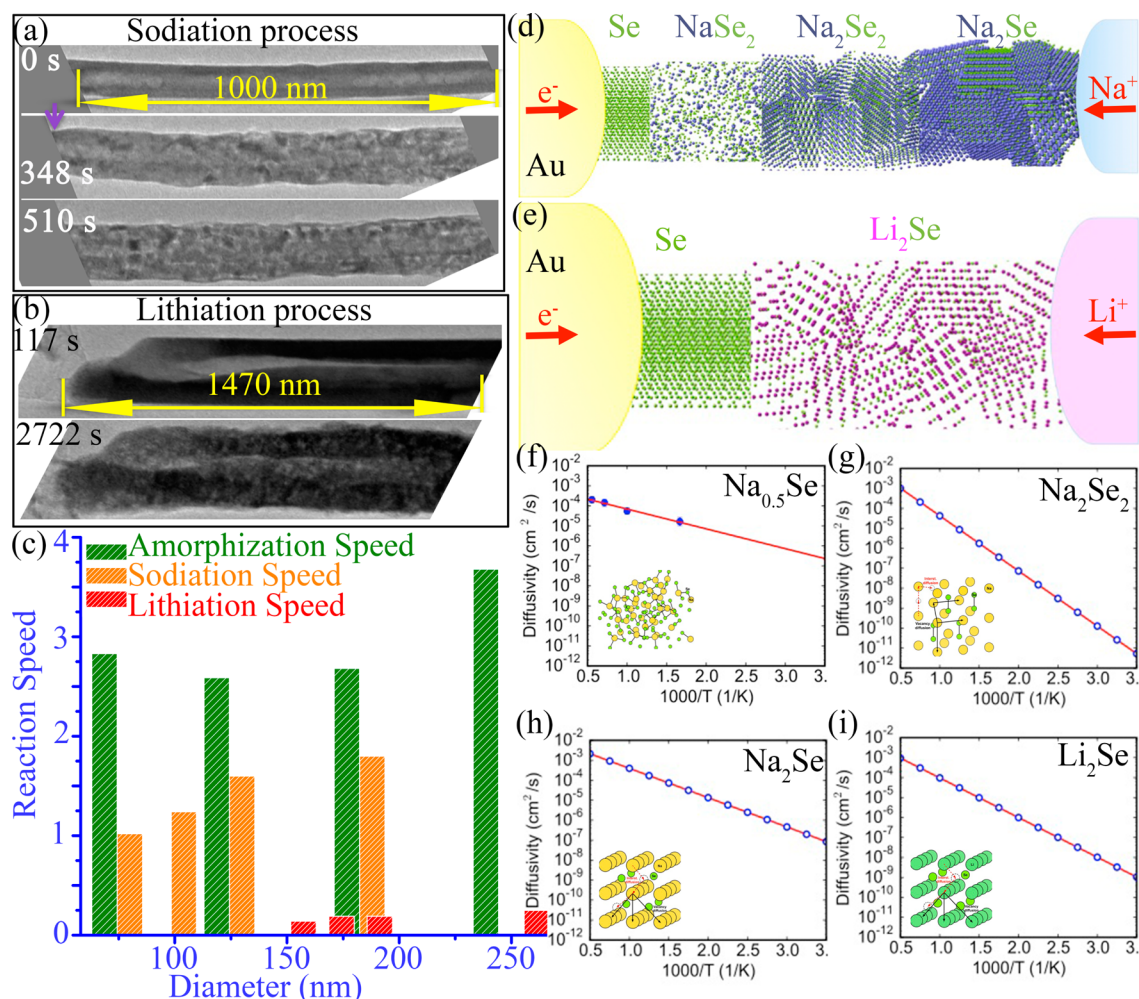


**Figure 5.** Reaction kinetics of a selenium nanotube in both sodiation and lithiation processes. (a) Sodiation of the selenium nanotube in 510 s. In the first stage of sodiation (solid-state amorphization), the reaction interface propagates at a mean speed of  $\sim 2.83 \text{ nm s}^{-1}$ . The overall propagation speed in the whole sodiation process is  $\sim 1.9 \text{ nm s}^{-1}$ . (b) Lithiation of the Se nanotube in 2722 s, with the mean lithiation speed is  $\sim 0.5 \text{ nm s}^{-1}$ . (c) Plot of the reaction speed versus diameters of several selenium nanotubes in both sodiation and lithiation processes. (d,e) Schematic illustration of sodiation and lithiation of selenium nanotubes. Three different phases appeared in sodiation due to the alloying reaction. In lithiation, selenium transforms to polycrystalline  $\text{Li}_2\text{Se}$  phase. (f–i) Arrhenius plot of the overall diffusion coefficient of the Na ion in the Na–Se phases and the Li ion in the  $\text{Li}_2\text{Se}$  phase through a vacancy mechanism.

and the crystal plane intensity of the experimental data matches well with the theoretical simulation shown in Figure S6. EDS maps of the three phases and the corresponding Na/Se ratios are shown in Figure 4a. We use the  $\text{Na}_2\text{Se}_2$  phase as a calibration to calculate the composition of the amorphous phase  $\text{Na}_x\text{Se}$ . The  $x$  is found to be about  $0.5 \pm 0.1$ , and the stoichiometry of the amorphous phase is then identified as  $\text{Na}_{0.5}\text{Se}$ , with the atomic ratio of Na to Se being 1:2. With DFT simulation, one of the stable intermediate Se–Na phases is found to be  $\text{Na}_{0.5}\text{Se}$  phase (in Figure S2), which matches the measured value of  $x$ . A structural model of the amorphous  $\text{Na}_{0.5}\text{Se}$  is then generated from the crystalline  $\text{NaSe}_2$  phase and is shown in Figure 4a, along with  $\text{Na}_2\text{Se}_2$  and  $\text{Na}_2\text{Se}$  phases. The atomic structural model of the amorphous  $\text{Na}_{0.5}\text{Se}$  structure is generated by relaxing its corresponding crystalline structure, as demonstrated in Figure S3a, and its corresponding radius distribution function is shown in Figure S3b.

The reaction kinetics of the selenium nanotube with sodium and lithium were then studied under similar experimental settings. We have found that the sodiation is almost 4–5 times faster than lithiation. Due to clear contrast interfaces among

different phases, the kinetics of the electrochemical reactions is monitored by measuring the moving speed of the phase interface through real-time TEM imaging. Figure 5a shows the first sodiation of a selenium nanotube with a length of 1000 nm. As the first stage of sodiation, a solid-state amorphization process on this nanotube takes about 348 s, with the propagation speed of the reaction front region of  $\sim 2.83 \text{ nm s}^{-1}$  (with volumetric speed of  $2 \times 10^4 \text{ nm}^3 \text{ s}^{-1}$ ). The recrystallization process takes about 510 s. Thus, the mean sodiation speed observed is about  $1.9 \text{ nm s}^{-1}$  (with volumetric speed of  $6 \times 10^4 \text{ nm}^3 \text{ s}^{-1}$ ). We have tested several nanotubes with different diameters. The overall sodiation speed against the nanotube diameters is shown by yellow bars in Figure 5c. In all of the measurements, the solid-state amorphization process as the first step of sodiation is fastest with an average speed of  $\sim 2.6 \text{ nm s}^{-1}$ , as shown by green bars in Figure 5c. The mean speed of the overall sodiation in these Se tubes is  $\sim 1.5 \text{ nm s}^{-1}$ . In comparison, the lithiation process takes almost 2722 s in the Se nanotube with a length of 1470 nm, indicating that the average lithiation speed is  $\sim 0.5 \text{ nm s}^{-1}$  (in Figure 5b). The lithiation has also been measured with other Se nanotubes, and

the results are shown by a red bar in Figure 5c, where the average speed is  $\sim 0.23 \text{ nm s}^{-1}$  (with volumetric speed of  $7 \times 10^3 \text{ nm}^3 \text{ s}^{-1}$ ) with the nanotube diameter ranging from 130 to 250 nm. In general, the overall sodiation of Se nanotubes is nearly 4–5 times faster than lithiation, while the solid-state amorphization as the first step of sodiation is even faster.

*Ab initio* molecular dynamics (MD) simulations and kinetic Monte Carlo simulations with nudged elastic band (NEB) method implemented are applied to understand the underlying mechanism of the electrochemical reaction of Se with Na and Li and their reaction kinetics. Using the DFT energies of known compounds available in the Open Quantum Materials Database<sup>18,19</sup> for the Na(Li)–Se system,<sup>20</sup> the ground-state phase diagrams are constructed, as shown in Figure S2. The stable compounds in the binary phase diagram refer to those which have lower energy than any linear combination of other compounds. According to the DFT calculations,  $\text{Li}_2\text{Se}$  is the only ground-state phase in the Li–Se binary systems, while in Na–Se systems, three phases ( $\text{NaSe}_2$ ,  $\text{Na}_2\text{Se}_2$ , and  $\text{Na}_2\text{Se}$ ) are found to be the ground-state phases. This explains why a three-step reaction mechanism has been observed in the sodiation, while only a single-step reaction has been observed for lithiation. Accordingly, in the calculated discharge profile, there is only one plateau in the lithiation, while three plateaus appear upon sodiation, as shown in Figure S4a. The calculated discharge profile also matches the measured one,<sup>12</sup> except there is a large overpotential for the Na-ion battery, which could be due to cell resistance.

To further explore the kinetics of reactions with sodium and lithium, reaction thermodynamics and electronic and ionic diffusivities are calculated by DFT. As shown in Figure S4b, the reaction energy between sodium and selenium ( $-3.441 \text{ eV}$ ) is slightly lower than that between lithium and selenium ( $-3.795 \text{ eV}$ ). This implies that although the diameter of the sodium ion ( $0.95 \text{ \AA}$ ) is much larger than that of lithium ion ( $0.68 \text{ \AA}$ ), the chemical activity of sodium is actually very close to that of lithium. This suggests that the difference in lithiation and sodiation speed should be mainly due to the kinetics of these reactions. The band gaps and ionic diffusivities in the Na–Se and Li–Se alloy phases have been calculated using first-principles calculations, with the results being listed in Table S1 and Figure 5f–i. Band gaps of all Na–Se intermediate phases are lower than that of the  $\text{Li}_2\text{Se}$ , suggesting that electrical conductivities of all the Na–Se intermediate phases are much better than that of the Li–Se intermediate phases. Meanwhile, the ionic diffusivity of sodium ions in all Na–Se alloying phases has also been calculated, and the results are shown in Figure 5f–i. The ionic conductivity of the amorphous  $\text{Na}_{0.5}\text{Se}$  phase ( $3.3 \times 10^{-7} \text{ cm}^2 \text{ s}^{-1}$ ) for Na ions is almost 2 orders higher than that of  $\text{Li}_2\text{Se}$  phase ( $2.2 \times 10^{-9} \text{ cm}^2 \text{ s}^{-1}$ ) for Li ions. Therefore, the higher kinetics in the sodiation reaction is caused by the better electric conductivity and higher  $\text{Na}^+$  mobility in the Na–Se alloying phases, compared to that of  $\text{Li}_2\text{Se}$  phase. Figure 5c schematically describes the phase transformations in both sodiation and lithiation processes. The sodiation was initialized with a solid-state amorphization process with formation of an amorphous  $\text{Na}_{0.5}\text{Se}$  phase, and the amorphous phase is gradually reduced to polycrystalline  $\text{Na}_2\text{Se}_2$  and  $\text{Na}_2\text{Se}$  crystalline phases. It is intriguing that selenium is reduced to an amorphous sodium polyselenide  $\text{Na}_{0.5}\text{Se}$  phase, instead of forming the crystalline  $\text{NaSe}_2$  phase. This could be due to fast insertion of sodium ions, leaving no time for the amorphous phase to relax to its ground-state phase.

## CONCLUSIONS

In summary, the reaction mechanism and kinetics of lithium/sodium with selenium, as the cathode material for both sodium- and lithium-ion batteries, are investigated at nanoscale in real time by *in situ* TEM. Selenium has alloying reactions with both Na and Li. Selenium is reduced to amorphous  $\text{Na}_{0.5}\text{Se}$ , polycrystalline  $\text{Na}_2\text{Se}_2$ , and  $\text{Na}_2\text{Se}$  sequentially in sodiation. The solid-state amorphization with the formation of  $\text{Na}_{0.5}\text{Se}$  accompanies a volume expansion of 58%, while the recrystallization with formation of  $\text{Na}_2\text{Se}_2$  and  $\text{Na}_2\text{Se}$  has a volume expansion about 336%. In lithiation, Se is directly reduced into the  $\text{Li}_2\text{Se}$  phase. Kinetics of the electrochemical reaction of Na/Se and Li/Se has been systematically investigated by monitoring the mobility of the reaction front interfaces. In general, Se nanotube sodiation is 4–5 times faster than lithiation, while the solid-state amorphization process is 10 times higher than lithiation, due to high electronic conductivity and ionic diffusivity of the intermediate Na–Se alloy phases produced in sodiation. DFT calculation shows that the Na–Se compounds that appeared in sodiation have narrow band gaps, thus high electronic conductivity and fast diffusion channels for sodium ions. Our finding shows that selenium is a promising high rate capability cathodic material for sodium-ion batteries. The investigation provides the insights to understand the sodiation and lithiation kinetics, which is helpful to design advanced-type sodium-ion batteries in the future.

## METHODS

**Synthesis of Selenium Nanotubes.** All chemicals were purchased from Sigma-Aldrich and used as received without any further purification. Selenium nanostructures were successfully synthesized by the aqueous solution method in recent years.<sup>21–23</sup> In our work, a selenium nanotube was prepared by a standard hydrothermal method based on some similar solution reaction methods. In this convenient approach of synthesizing selenium nanotubes, 0.52 g of  $\text{Na}_2\text{SeO}_3$  and 2 g of glucose were dissolved in 50 mL of distilled water in a beaker. After being magnetically stirred for 30 min, the solution was transferred into two 25 mL Teflon-lined stainless steel autoclaves and sealed at room temperature. We placed the autoclaves into an oven and heated them to  $90 \text{ }^\circ\text{C}$  for 2 h, then we took the autoclaves out and cooled them quickly to room temperature in water. The product was collected by filtration and repeated washing with acetone and distilled water and then dried in an oven at  $90 \text{ }^\circ\text{C}$ . The chemical reaction involved in our method is  $\text{Na}_2\text{SeO}_3 + 2\text{C}_6\text{H}_8\text{O}_6 \rightarrow \text{Se} + 2\text{NaC}_4\text{H}_4\text{O}_6 + 3\text{H}_2\text{O}$ , and then high-quality selenium nanotubes were obtained in a high yield with eco-friendly chemicals and simple equipment.

**Nanobattery Setup.** The sodiation and lithiation reaction were conducted inside TEM by the nanobattery setup on the Nanofactory holder, as designed in previous reports.<sup>24–29</sup> Selenium nanotubes were pasted on one end of the Au rod with conductive epoxy and used as cathode materials. Lithium and sodium metals were sketched by a tungsten probe and acted as the counter electrode in the lithium- and sodium-ion batteries, respectively. The solid electrolytes used in the *in situ* TEM experiments consist mainly of  $\text{Li}_2\text{O}$  and  $\text{Na}_2\text{O}$ , respectively, for Li and Na lithiation. The compact  $\text{Li}_2\text{O}$  film has a thickness of about 72–115 nm and high Li-ion conductivity with Li-ion diffusion activation energy of about 0.21–0.31 eV (Figure S8a,c). The porous  $\text{Na}_2\text{O}/\text{NaOH}$  film has a thickness of about 173–216 nm and high Na-ion conductivity with Na-ion diffusion activation energy of about 0.15 eV (Figure S8b,d). We accurately controlled the counter electrode to touch the selenium working electrode, then sodiation and desodiation experiments could be conducted by applying different potentiostatic holds of the working electrode with respect to the counter electrode. The morphology and microstructure evolutions were studied by the *in*

*situ* TEM image mode and *in situ* electron diffraction patterns in real time.

**First-Principles Simulation of Sodiation and Lithiation of Selenium.** The first-principles DFT calculations were conducted through the Vienna *ab initio* simulation package (VASP).<sup>30–33</sup> With the projector-augmented wave potentials,<sup>34</sup> generalized gradient approximation of Perdew–Becke–Ernzerhof<sup>35</sup> was used for the exchange–correlation function by considering spin-polarization. A plane-wave basis set cutoff energy of 520 eV and  $\Gamma$ -centered  $k$ -meshes with a density of 8000  $k$ -points per reciprocal atom were used in all calculations.

To create a supercell of amorphous Na<sub>0.5</sub>Se suitable for DFT calculations, a cell containing 96 atoms was melted at 2900 K in *ab initio* molecular dynamics. The liquid-state configuration was equilibrated over 2 ps under an NVT ensemble,<sup>36</sup> followed by a rapid quench from the equilibration temperature to 300 K at a rate of 1 K fs<sup>−1</sup>. Then the atomic coordinates and cell parameters of the configuration were relaxed in DFT until the average forces fall below 10<sup>−2</sup> eV Å<sup>−1</sup>.<sup>37</sup>

In order to simulate the Na (Li)-ion diffusions in selenium during the sodiation (lithiation), different first-principles methods were applied to evaluate the ion transport through different kinetic mechanisms. For ion self-diffusions by vacancies, kinetic Monte Carlo simulation was conducted based on transition-state theory. The rate of jumps from site  $i$  to site  $j$  was obtained by

$$R_{ij} = \nu_{ij} \exp(-\Delta H_{ij}^{\text{mig}}/k_{\text{B}}T)$$

where  $\nu_{ij}$  is the attempt frequency for the jump and  $\Delta H_{ij}^{\text{mig}}$  is the enthalpy difference of the system between ground and transition states at  $T = 0$  K. Theoretically, the attempt frequency can be evaluated with harmonic vibrational modes of the defected system in both ground and transition states. Nevertheless, we have not conducted such calculations in the current work, and we chose constant  $\nu_{ij} = 10^{13}$  s<sup>−1</sup>. Since  $\nu_{ij}$  is independent of temperature in the classical limit, this choice will have a negligible effect on activation energy calculations. In each simulation, displacement vector,  $d$ , was calculated by the difference between the initial and final positions of the defect. The diagonal elements of the diffusivity tensor were then evaluated by

$$D_{\gamma\gamma} = \frac{\langle d_{\gamma}^2 \rangle}{2\langle \Delta t \rangle}$$

where  $d_{\gamma}$  is the component of the displacement vector in the  $\gamma$  direction ( $\gamma = x, y, \text{ or } z$ ) and  $\Delta t$  is the duration of a single simulation. Averages of  $d_{\gamma}$  and  $\Delta t$  were taken over all simulations at a certain temperature; these simulations were performed until the standard error was within 1% of the mean diffusivity at that temperature. Then diffusivity was calculated with 10 K intervals using isolated defects in an infinite crystal to simulate diffusion in the bulk. NEB calculations were performed to obtain each diffusion path, and climbing image NEB calculations were performed to find the barriers needed for the kinetic Monte Carlo simulations. NEB calculations were performed using VTST tools.<sup>38,39</sup> For ion diffusions through interstitial mechanisms, *ab initio* MD simulations were performed in VASP using supercells consisting of 96 (96, 81, and 81) atoms for NaSe<sub>2</sub>, (Na<sub>2</sub>Se<sub>2</sub>, Na<sub>2</sub>Se, and Li<sub>2</sub>Se). We simulated the canonical (NVT) ensemble through a Nose thermostat with a minimal  $\Gamma$ -centered  $1 \times 1 \times 1$   $k$ -point grid.<sup>40,41</sup> In each run, velocity–Verlet was used for a time integration scheme with a step of 2 fs. Considering thermal expansion, we conducted a series of volume-varying picosecond runs at each target temperature. Therefore, the volume of the supercell was determined, where the average pressure was approximately zero. When the MD simulations started, the Na(Li)–Se systems were assigned an initial temperature of 100 K, and it was heated to target temperatures (600–1800 K) in 2 ps and equilibrated for 5 ps. We performed MD simulations to conduct the diffusion for 40 ps.

In addition, Na (Li)-ion diffusivities at each target temperature were calculated by fitting the mean square displacement over time using the following equation:  $D = \frac{1}{2t} [r_c(t)]^2$ . Here,  $r(t)$  is the displacement of

ions at time  $t$  and  $D$  was obtained by a linear fitting to the dependence of average mean square displacement over  $2t$ .

## ASSOCIATED CONTENT

### Supporting Information

The Supporting Information is available free of charge on the ACS Publications website at DOI: 10.1021/acsnano.6b04519.

Seven supplementary figures and one supplementary table (PDF)

Movie S1 (MPG)

Movie S2 (AVI)

Movie S3 (MPG)

Movie S4 (MPG)

## AUTHOR INFORMATION

### Corresponding Authors

\*E-mail: jinsong-wu@northwestern.edu.

\*E-mail: v-dravid@northwestern.edu.

### Notes

The authors declare no competing financial interest.

## ACKNOWLEDGMENTS

This work was supported as part of the Center for Electrochemical Energy Science, an Energy Frontier Research Center funded by the U.S. Department of Energy (DOE), Office of Science, Basic Energy Sciences under Award No. DEAC02-06CH11357, and the Initiative for Sustainability and Energy at Northwestern (ISEN). This work was also supported by the NUANCE Center at Northwestern University, using the EPIC facility that receives support from the Soft and Hybrid Nanotechnology Experimental (SHyNE) Resource (NSF NNCI-1542205); the MRSEC program (NSF DMR-1121262) at the Materials Research Center; the International Institute for Nanotechnology (IIN); the Keck Foundation; and the State of Illinois, through the IIN. We gratefully acknowledge the computing resources from (1) the National Energy Research Scientific Computing Center, a DOE Office of Science User Facility supported by the Office of Science of the U.S. Department of Energy under Contract DE-AC02-05CH11231, and (2) Blues, a high-performance computing cluster operated by the Laboratory Computing Resource Center at Argonne National Laboratory.

## REFERENCES

- (1) Kim, D.; Kang, S. H.; Slater, M.; Rood, S.; Vaughey, J. T.; Karan, N.; Balasubramanian, M.; Johnson, C. S. Enabling Sodium Batteries Using Lithium-Substituted Sodium Layered Transition Metal Oxide Cathodes. *Adv. Energy Mater.* **2011**, *1*, 333–336.
- (2) Komaba, S.; Murata, W.; Ishikawa, T.; Yabuuchi, N.; Ozeki, T.; Nakayama, T.; Ogata, A.; Gotoh, K.; Fujiwara, K. Electrochemical Na Insertion and Solid Electrolyte Interphase for Hard-Carbon Electrodes and Application to Na-Ion Batteries. *Adv. Funct. Mater.* **2011**, *21*, 3859–3867.
- (3) Larcher, D.; Tarascon, J. Towards Greener and More Sustainable Batteries for Electrical Energy Storage. *Nat. Chem.* **2015**, *7*, 19–29.
- (4) Yang, Z.; Zhang, J.; Kintner-Meyer, M. C. W.; Lu, X.; Choi, D.; Lemmon, J. P.; Liu, J. Electrochemical Energy Storage for Green Grid. *Chem. Rev.* **2011**, *111*, 3577–3613.
- (5) Lu, X.; Li, G.; Kim, J. Y.; Mei, D.; Lemmon, J. P.; Sprenkle, V. L.; Liu, J. Liquid-Metal Electrode to Enable Ultra-Low Temperature Sodium–Beta Alumina Batteries for Renewable Energy Storage. *Nat. Commun.* **2014**, *5*, 4578.

- (6) Lu, X.; Bowden, M. E.; Sprenkle, V. L.; Liu, J. A Low Cost, High Energy Density, and Long Cycle Life Potassium–Sulfur Battery for Grid-Scale Energy Storage. *Adv. Mater.* **2015**, *27*, 5915–5922.
- (7) Sudworth, J. L.; Tilley, A. *The Sodium Sulfur Battery*; Kluwer Academic Publishers, 1985.
- (8) Sauvage, F.; Baudrin, E.; Tarascon, J.-M. Study of the Potentiometric Response towards Sodium Ions of  $\text{Na}_{0.44-x}\text{MnO}_2$  for the Development of Selective Sodium Ion Sensors. *Sens. Actuators, B* **2007**, *120*, 638–644.
- (9) Wenzel, S.; Hara, T.; Janek, J.; Adelhelm, P. Room-Temperature Sodium-Ion Batteries: Improving the Rate Capability of Carbon Anode Materials by Templating Strategies. *Energy Environ. Sci.* **2011**, *4*, 3342–3345.
- (10) Sun, J.; Lee, H.-W.; Pasta, M.; Yuan, H.; Zheng, G.; Sun, Y.; Li, Y.; Cui, Y. A Phosphorene–Graphene Hybrid Material as a High-Capacity Anode for Sodium-Ion Batteries. *Nat. Nanotechnol.* **2015**, *10*, 980–985.
- (11) Fan, X.; Mao, J.; Zhu, Y.; Luo, C.; Suo, L.; Gao, T.; Han, F.; Liou, S. C.; Wang, C. Superior Stable Self-Healing  $\text{SnP}_3$  Anode for Sodium-Ion Batteries. *Adv. Energy Mater.* **2015**, *5*, 1500174.
- (12) Abouimrane, A.; Dambournet, D.; Chapman, K. W.; Chupas, P. J.; Weng, W.; Amine, K. A New Class of Lithium and Sodium Rechargeable Batteries Based on Selenium and Sulfur as a Positive Electrode. *J. Am. Chem. Soc.* **2012**, *134*, 4505–4508.
- (13) Cui, Y.; Abouimrane, A.; Lu, J.; Bolin, T.; Ren, Y.; Weng, W.; Sun, C.; Maroni, V. A.; Heald, S. M.; Amine, K. (De) Lithiation Mechanism of  $\text{Li}/\text{SeS}_x$  ( $x = 0-7$ ) Batteries Determined by *In Situ* Synchrotron X-ray Diffraction and X-ray Absorption Spectroscopy. *J. Am. Chem. Soc.* **2013**, *135*, 8047–8056.
- (14) Zeng, L.; Zeng, W.; Jiang, Y.; Wei, X.; Li, W.; Yang, C.; Zhu, Y.; Yu, Y. A Flexible Porous Carbon Nanofibers–Selenium Cathode with Superior Electrochemical Performance for Both Li–Se and Na–Se Batteries. *Adv. Energy Mater.* **2015**, *5*, 1401377.
- (15) Luo, C.; Xu, Y.; Zhu, Y.; Liu, Y.; Zheng, S.; Liu, Y.; Langrock, A.; Wang, C. Selenium@ Mesoporous Carbon Composite with Superior Lithium and Sodium Storage Capacity. *ACS Nano* **2013**, *7*, 8003–8010.
- (16) Luo, C.; Zhu, Y.; Wen, Y.; Wang, J.; Wang, C. Carbonized Polyacrylonitrile-Stabilized  $\text{SeS}_x$  Cathodes for Long Cycle Life and High Power Density Lithium Ion Batteries. *Adv. Funct. Mater.* **2014**, *24*, 4082–4089.
- (17) Yang, C. P.; Xin, S.; Yin, Y. X.; Ye, H.; Zhang, J.; Guo, Y. G. An Advanced Selenium–Carbon Cathode for Rechargeable Lithium–Selenium Batteries. *Angew. Chem., Int. Ed.* **2013**, *52*, 8363–8367.
- (18) Saal, J. E.; Kirklin, S.; Aykol, M.; Meredig, B.; Wolverton, C. Materials Design and Discovery with High-Throughput Density Functional Theory: The Open Quantum Materials Database (OQMD). *JOM* **2013**, *65*, 1501–1509.
- (19) Kirklin, S.; Saal, J. E.; Meredig, B.; Thompson, A.; Doak, J. W.; Aykol, M.; Rühl, S.; Wolverton, C. The Open Quantum Materials Database (OQMD): Assessing the Accuracy of DFT Formation Energies. *npj Comput. Mater.* **2015**, *1*, 15010.
- (20) Sangster, J.; Pelton, A. The Na–Se (Sodium–Selenium) System. *J. Phase Equilib.* **1997**, *18*, 185–189.
- (21) Cheng, B.; Samulski, E. T. Rapid, High Yield, Solution-Mediated Transformation of Polycrystalline Selenium Powder into Single-Crystal Nanowires. *Chem. Commun.* **2003**, 2024–2025.
- (22) Chen, H.; Shin, D.-W.; Nam, J.-G.; Kwon, K.-W.; Yoo, J.-B. Selenium Nanowires and Nanotubes Synthesized via a Facile Template-Free Solution Method. *Mater. Res. Bull.* **2010**, *45*, 699–704.
- (23) Li, Q.; Yam, V. W.-W. High-Yield Synthesis of Selenium Nanowires in Water at Room Temperature. *Chem. Commun.* **2006**, 1006–1008.
- (24) He, K.; Zhou, Y.; Gao, P.; Wang, L.; Pereira, N.; Amatucci, G. G.; Nam, K.-W.; Yang, X. Q.; Zhu, Y.; Wang, F.; et al. Sodiation via Heterogeneous Disproportionation in  $\text{FeF}_2$  Electrodes for Sodium-Ion Batteries. *ACS Nano* **2014**, *8*, 7251–7259.
- (25) Li, Q.; Wang, P.; Feng, Q.; Mao, M.; Liu, J.; Mao, S. X.; Wang, H. *In Situ* TEM on The Reversibility of Nanosized Sn Anodes during The Electrochemical Reaction. *Chem. Mater.* **2014**, *26*, 4102–4108.
- (26) Li, Q.; Wang, P.; Feng, Q.; Mao, M.; Liu, J.; Wang, H.; Mao, S. X.; Zhang, X.-X. Superior Flexibility of a Wrinkled Carbon Shell under Electrochemical Cycling. *J. Mater. Chem. A* **2014**, *2*, 4192–4197.
- (27) Li, Q.; Li, W.; Feng, Q.; Wang, P.; Mao, M.; Liu, J.; Zhou, L.; Wang, H.; Yao, H. Thickness-Dependent Fracture of Amorphous Carbon Coating on  $\text{SnO}_2$  Nanowire Electrodes. *Carbon* **2014**, *80*, 793–798.
- (28) Luo, L.; Wu, J.; Xu, J.; Dravid, V. P. Atomic Resolution Study of Reversible Conversion Reaction in Metal Oxide Electrodes for Lithium-Ion Battery. *ACS Nano* **2014**, *8*, 11560–11566.
- (29) Nie, A.; Gan, L.-Y.; Cheng, Y.; Li, Q.; Yuan, Y.; Mashayek, F.; Wang, H.; Klie, R.; Schwingenschlogl, U.; Shahbazian-Yassar, R. Twin Boundary-Assisted Lithium Ion Transport. *Nano Lett.* **2015**, *15*, 610–615.
- (30) Kresse, G.; Hafner, J. *Ab Initio* Molecular Dynamics for Liquid Metals. *Phys. Rev. B: Condens. Matter Mater. Phys.* **1993**, *47*, 558–561.
- (31) Kresse, G.; Hafner, J. *Ab Initio* Molecular-Dynamics Simulation of the Liquid-Metal–Amorphous-Semiconductor Transition in Germanium. *Phys. Rev. B: Condens. Matter Mater. Phys.* **1994**, *49*, 14251–14269.
- (32) Kresse, G.; Furthmüller, J. Efficiency of *Ab-initio* Total Energy Calculations for Metals and Semiconductors Using a Plane-Wave Basis Set. *Comput. Mater. Sci.* **1996**, *6*, 15–50.
- (33) Kresse, G.; Furthmüller, J. Efficient Iterative Schemes for *Ab Initio* Total-Energy Calculations Using a Plane-Wave Basis Set. *Phys. Rev. B: Condens. Matter Mater. Phys.* **1996**, *54*, 11169–11186.
- (34) Blöchl, P. E. Projector Augmented-Wave Method. *Phys. Rev. B: Condens. Matter Mater. Phys.* **1994**, *50*, 17953–17979.
- (35) Perdew, J. P.; Ernzerhof, M.; Burke, K. Rationale for Mixing Exact Exchange with Density Functional Approximations. *J. Chem. Phys.* **1996**, *105*, 9982–9985.
- (36) Farrell, D. E.; Wolverton, C. Structure and Diffusion in Liquid Complex Hydrides via *Ab Initio* Molecular Dynamics. *Phys. Rev. B: Condens. Matter Mater. Phys.* **2012**, *86*, 174203.
- (37) Hao, S.; Wolverton, C. Lithium Transport in Amorphous  $\text{Al}_2\text{O}_3$  and  $\text{AlF}_3$  for Discovery of Battery Coatings. *J. Phys. Chem. C* **2013**, *117*, 8009–8013.
- (38) Henkelman, G.; Jónsson, H. Improved Tangent Estimate in the Nudged Elastic Band Method for Finding Minimum Energy Paths and Saddle Points. *J. Chem. Phys.* **2000**, *113*, 9978–9985.
- (39) Henkelman, G.; Uberuaga, B. P.; Jónsson, H. A Climbing Image Nudged Elastic Band Method for Finding Saddle Points and Minimum Energy Paths. *J. Chem. Phys.* **2000**, *113*, 9901–9904.
- (40) Nosé, S. A Unified Formulation of the Constant Temperature Molecular Dynamics Methods. *J. Chem. Phys.* **1984**, *81*, 511–519.
- (41) Nosé, S. Constant Temperature Molecular Dynamics Methods. *Prog. Theor. Phys. Suppl.* **1991**, *103*, 1–46.